

## SUPPORTING INFORMATION

### **Recyclable construction of multiple films with impedance gradient design for high-efficiency electromagnetic absorption performances**

Yu Chen,<sup>a</sup> Bin Quan,<sup>\*a</sup> Litao Lin,<sup>a</sup> Linyu Xie,<sup>d</sup> Haoyu Jiao,<sup>a</sup> Xinyi Min,<sup>c</sup> Gaoyuan Yu,<sup>a</sup> Binglin He,<sup>e</sup> Xiaochi Lu,<sup>b</sup> Jiajia Liu,<sup>a</sup> Yan Chen<sup>a</sup> and Xiaogu Huang<sup>\*a</sup>

<sup>a</sup>School of Chemistry and Materials Science, Nanjing University of Information Science & Technology, Nanjing, 210044, China.

<sup>b</sup>College of Electronic and Optical Engineering & College of Flexible Electronics (future Technology), Nanjing University of Posts and Telecommunications, Nanjing, 210023, China.

<sup>c</sup>JiangSu JACK Instrument Co.,Ltd, 211600, China.

<sup>d</sup>School of Communications and Information Engineering, Nanjing University of Posts and Telecommunications, 210023, China.

<sup>e</sup>School of Computer engineering, Tongda College of Nanjing University of Posts and Telecommunications, 225127, China.

† Corresponding Author, Prof. Bin Quan E-mail: [binquan@nuist.edu.cn](mailto:binquan@nuist.edu.cn)

Corresponding Author, Prof. Xiaogu Huang E-mail: [hxg@nuist.edu.cn](mailto:hxg@nuist.edu.cn)

## Experimental

### Preparation of TCF films

A reusable and flexible TPE/CNTs/Fe<sub>2</sub>O<sub>3</sub> film was fabricated using an evaporation drying technique. The resulting film not only exhibits excellent microwave absorption capabilities but also possessed the attribute of recyclability. The fabrication process is depicted in Fig. 1. In details, TPE (5000 mg, (C<sub>8</sub>H<sub>8</sub>.C<sub>4</sub>H<sub>6</sub>)<sub>n</sub>) was firstly added to cyclohexane (100 mL) at 80°C with continuous stirring for 1 h to obtain TPE solution. CNTs and  $\gamma$ -Fe<sub>2</sub>O<sub>3</sub> were dispersed in cyclohexane with ultrasonic processing for 2 h to obtain TPE/CNTs/Fe<sub>2</sub>O<sub>3</sub> mixture. Subsequently, the mixture was transferred into mould and dried at room temperature. Once the drying is completed, the film can be uncovered. The specific configuration is shown in Table 1, and the as-prepared samples are simplified as TCF1, TCF2, TCF3 and TCF4, respectively.

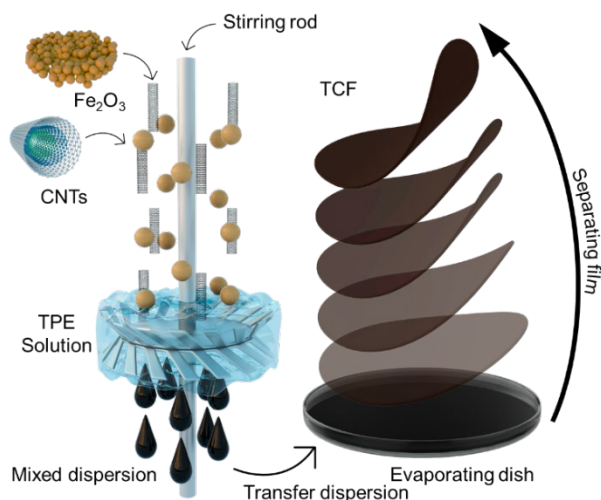


Fig. S1 Preparation diagram of TCF film.

Table 1. The filling ratio of different TCF films.

Sample	TPE / mg	CNTs / mg	$\gamma$ -Fe <sub>2</sub> O <sub>3</sub> / mg
TCF1	5000	200	500
TCF2	5000	200	2000
TCF3	5000	800	500
TCF4	5000	800	2000

### Characterization

The X-ray diffraction (XRD) patterns were detected by D/teX Ultra 250 detector (Rigaku Co.) with Cu K $\alpha$  ( $\lambda = 1.5406 \text{ \AA}$ ) radiation. The morphology of the materials was determined by scanning electron microscope (SEM, Hitachi SU8010). Thermogravimetric analysis was performed using PerkinElmer TGA 6000. The Lake Shore 8604 Model vibration sample magnetometer was used to characterize the hysteresis loop of the film. The EM parameters were recorded at 8.2-12.4 GHz by waveguide method using vector network analyser (VNA, Agilent PNA N5224A).

### Simulation

Simulation is a fast way to achieve material screening, which can provide guidance for the experiment. CST studio suit 2019 can be used to simulate the change in the electric field, the magnetic field and the S-parameter. To elucidate the behaviour of the TCF film within a waveguide cavity, a simulation was executed. The model is mainly based on the waveguide test method, which can obtain S-parameters compared with the structure with metal backplane. The stability of the multilayer film can be guaranteed when preparing the test sample. The simulation settings were based on the X-band waveguide shapes, with dimensions of 22.86 mm for the longer side and 10.16 mm for the shorter side. It is difficult to achieve precise thickness control of the films, the thickness used in the simulation is consistent with the actual thickness of the films to ensure the consistency between simulation and experiment. The simulated film's

total thickness was accurately set to 3.51 mm, segmented into four layers with thicknesses of 0.84 mm, 0.84 mm, 0.77 mm, and 1.06 mm. The two sides of the four layers film are surrounded by vacuum layers (5 mm). For 3.51 mm homogeneous film, the thickness of each layer is set to 0.8775 mm. The waveguide ports were configured at the vacuum interface at both ends, with the excitation source positioned at the waveguide port in the direction perpendicular to the z-axis. Both ports were designated as receiving ports. The simulation boundary is set as electrical boundary conditions and spans a frequency range from 8.2 to 12.4 GHz. E-field monitor, H-field monitor and Power loss density (PLD) monitor are settled to get simulation data.

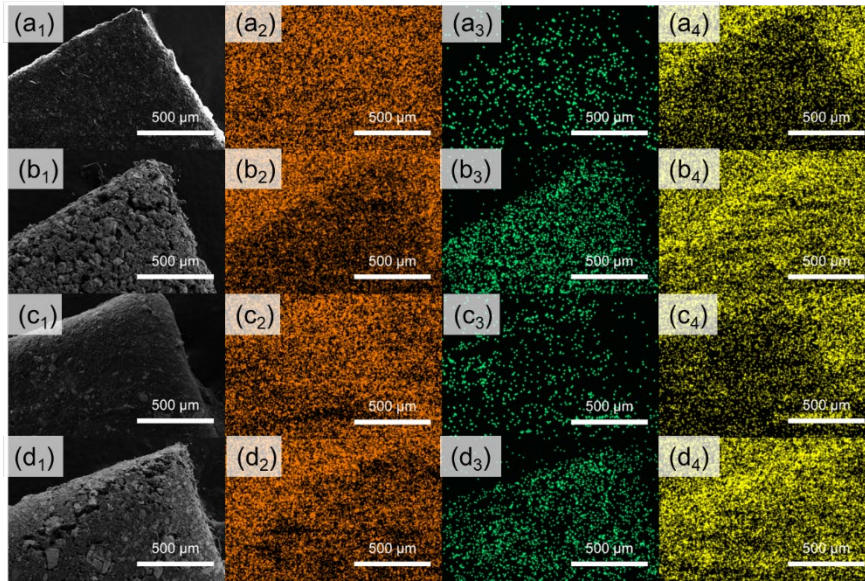


Fig. S2 SEM data. SEM images and EDS images of (g) TCF1, (h) TCF2, (i) TCF3, (j) TCF4. The subscript number corresponds to the (1) SEM image, (2) C element, (3) Fe element and (4) O element, respectively.

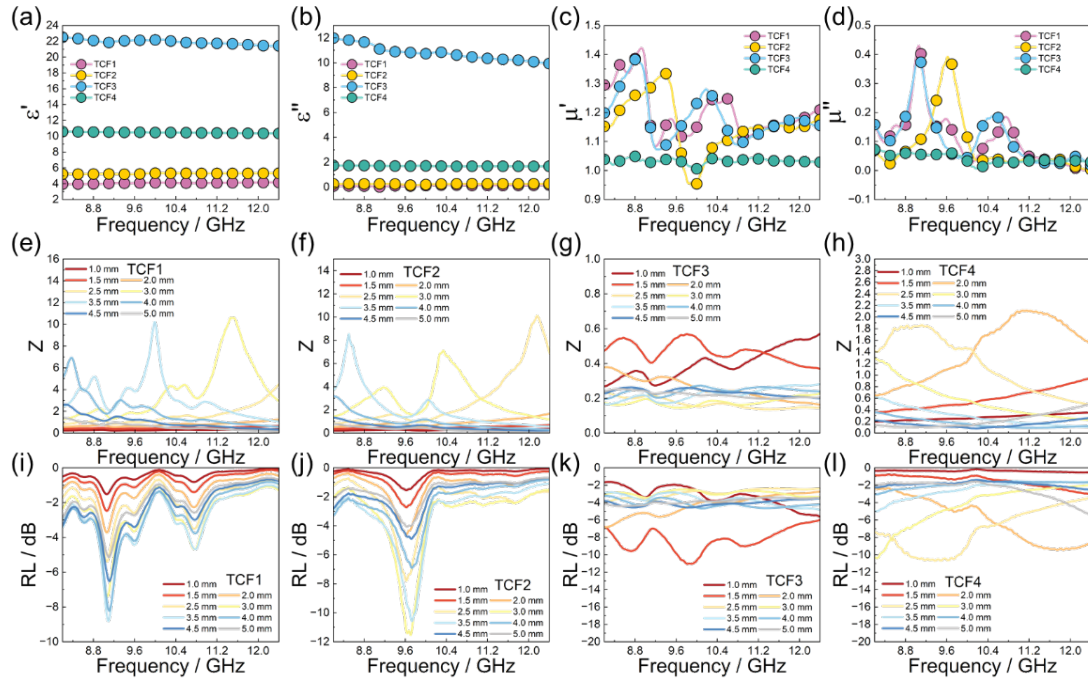


Fig. S3 EM properties of TCF1-4 films. (a) The real part of the dielectric, (b) the imaginary part of the dielectric; (c) The real part of the permeability and (d) the imaginary part of the permeability of the TCF1-4 film; (e-h) IM and (i-l) RL of TCF1-4 films.

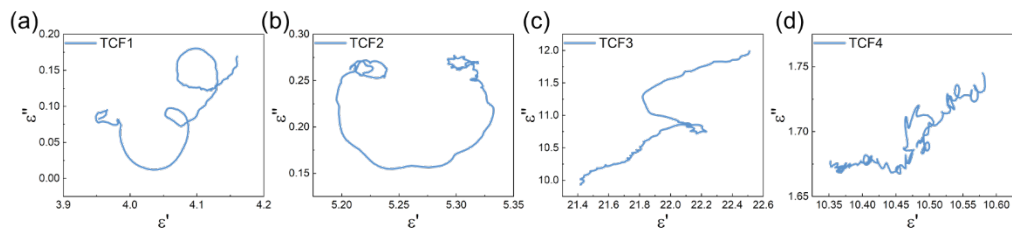


Fig. S4. Cole-Cole semicircles of TCF1, TCF2, TCF3 and TCF4.

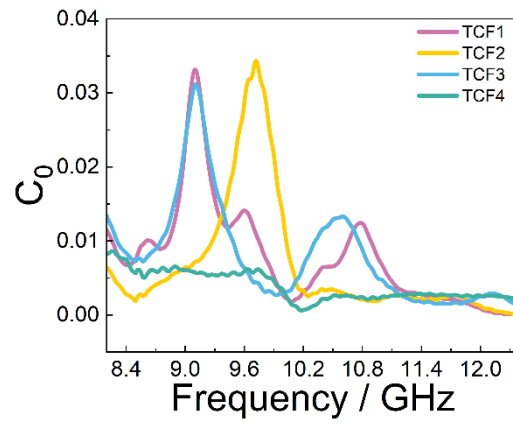


Fig. S5. Eddy current loss of TCF1, TCF2, TCF3 and TCF4.

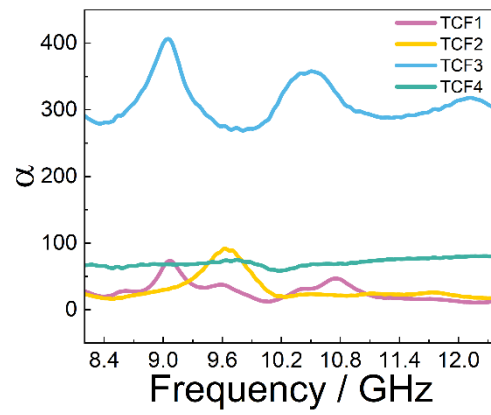


Fig. S6. Attenuation constant of TCF1, TCF2, TCF3 and TCF4.



Fig. S7 Reusable operations of the film: (a) mixing the wasted film, (b-c) transferring and dissolution.

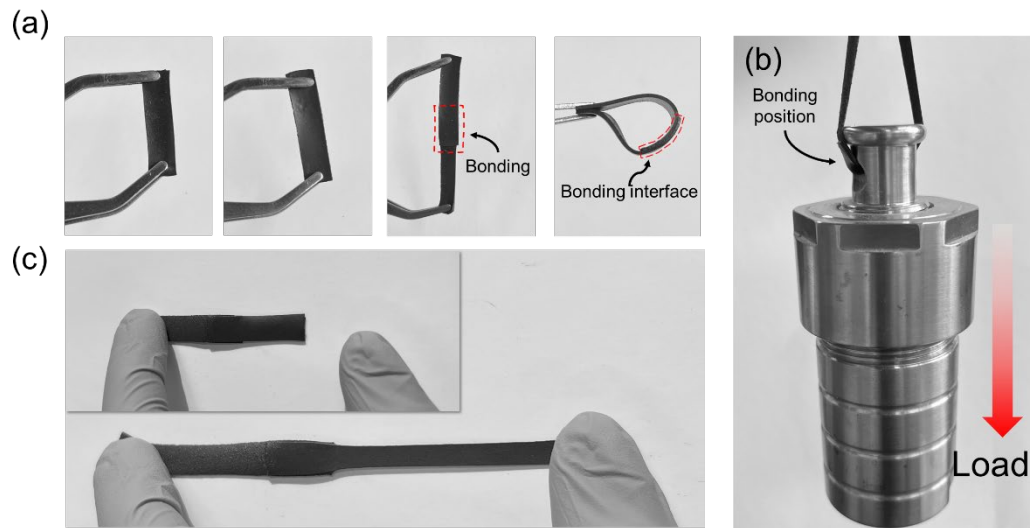


Fig. S8 (a) Actual pictures of TCF1 and TCF2 connection; (b) A load is added to connection. (c) The horizontal stretching state of TCF1 and TCF2 connection.

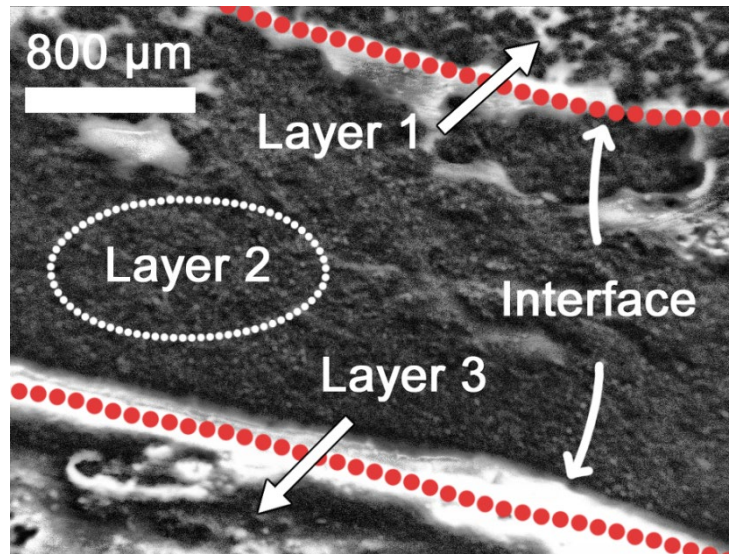


Fig. S9. SEM image at the interface of multilayer film.

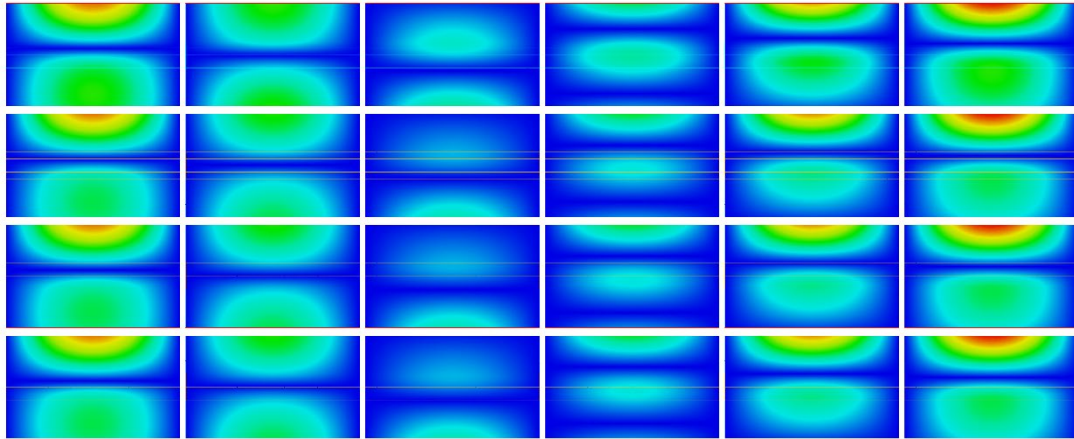


Fig. S10. The electric field diagrams for 1111, 2222, 3333, and 4444 are depicted from top to bottom. In the horizontal direction, the phase of the electric field ranges from  $0^\circ$  to  $150^\circ$  on the far left, with an increment of  $30^\circ$  between each graph.

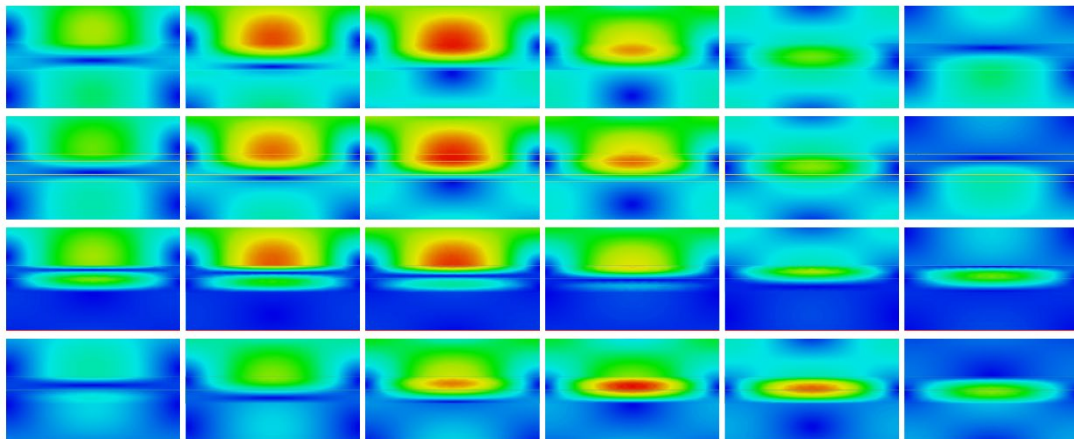


Fig. S11. The magnetic field diagrams for 1111, 2222, 3333, and 4444 are depicted from top to bottom. In the horizontal direction, the phase of the magnetic field ranges from  $0^\circ$  to  $150^\circ$  on the far left, with an increment of  $30^\circ$  between each graph.

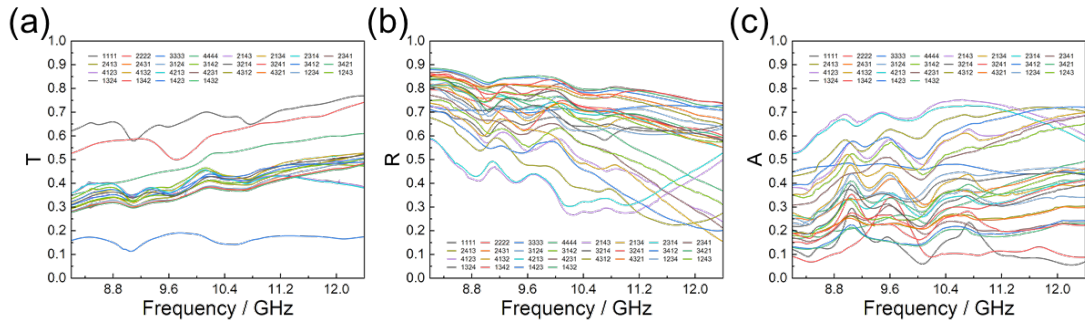


Fig. S12. S parameters of multiple films with random assortment between four single films.

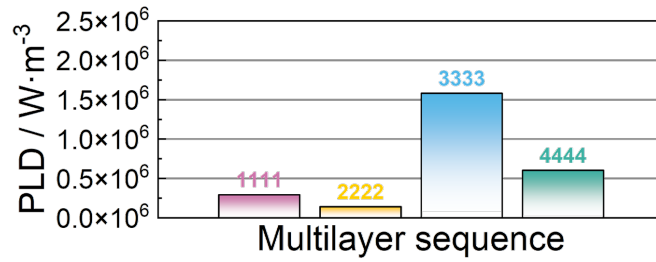


Fig. S13 The PLD<sub>max</sub> of initial TCF film

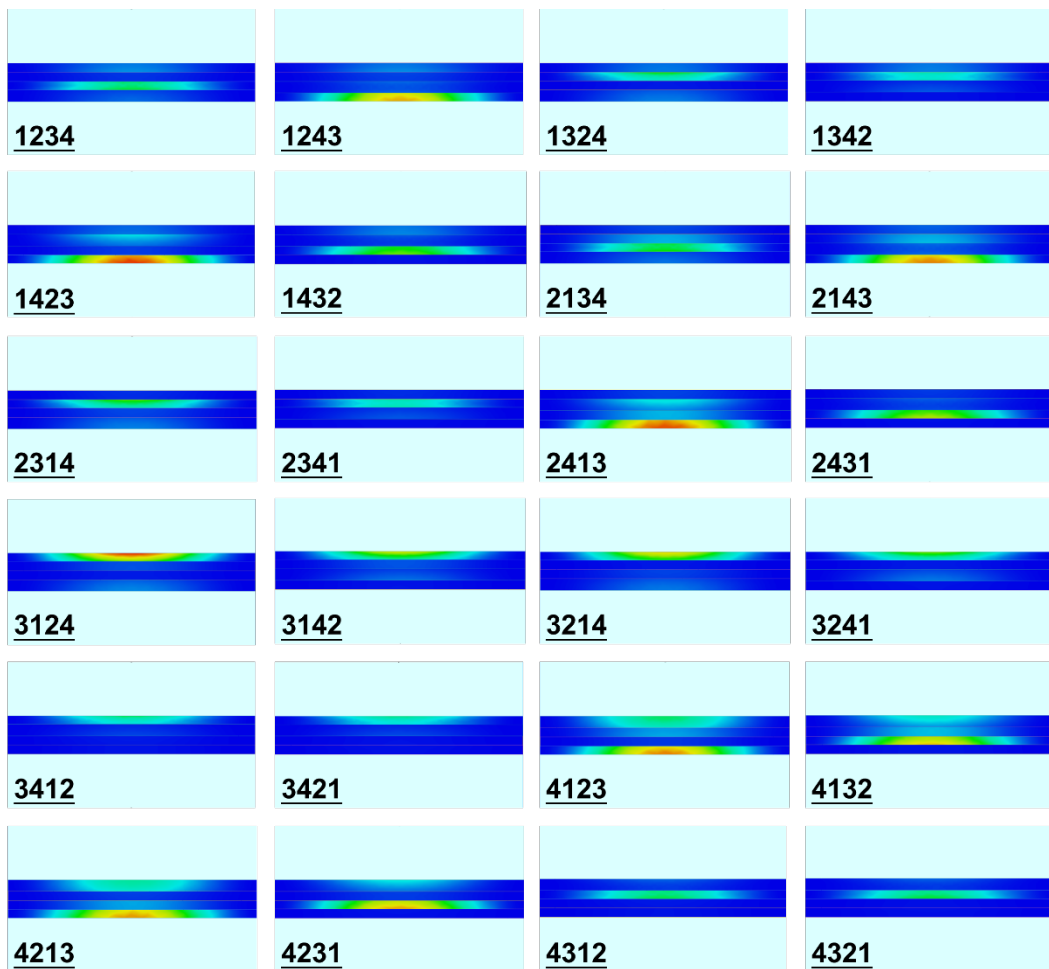


Fig. S14. PLD value images of multiple films with random assortment between four single films.

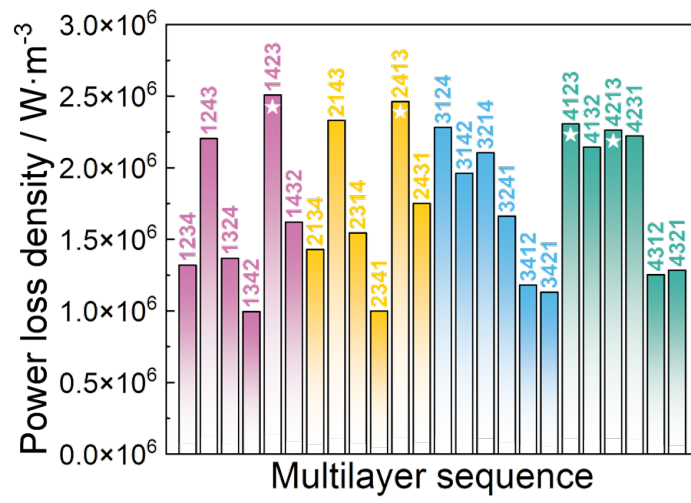


Fig. S15 The PLD<sub>max</sub> of 24 kinds of composite films.

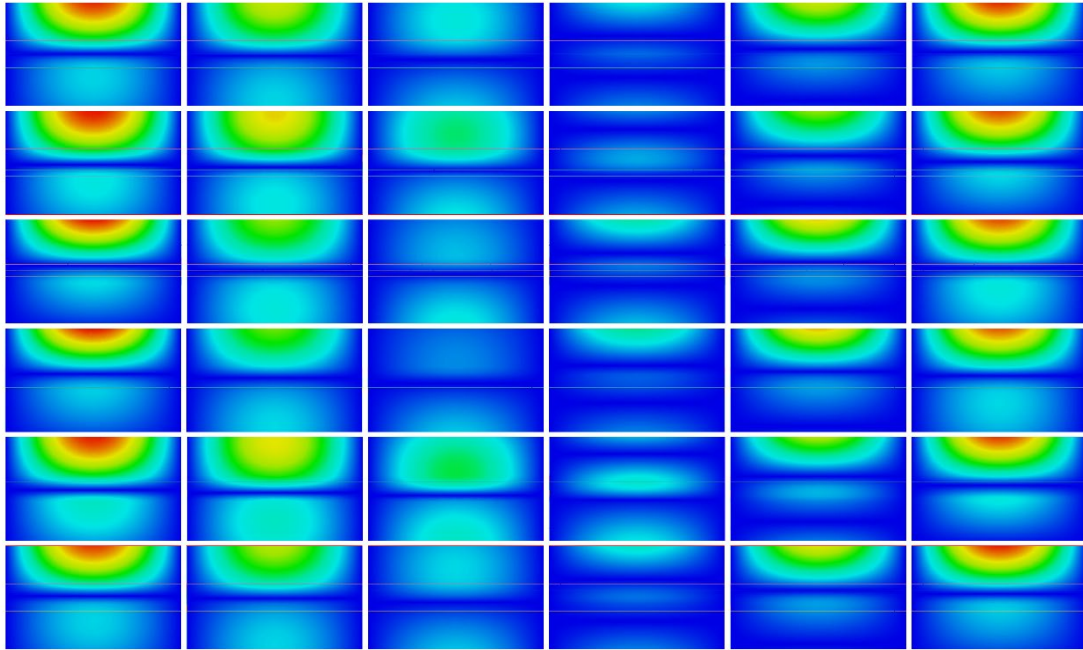


Fig. S16. The electric field diagrams for TCF1234, TCF1243, TCF1324, TCF1342, TCF1423, and TCF1432 are depicted from top to bottom. In the horizontal direction, the phase of the electric field ranges from  $0^\circ$  to  $150^\circ$  on the far left, with an increment of  $30^\circ$  between each graph.

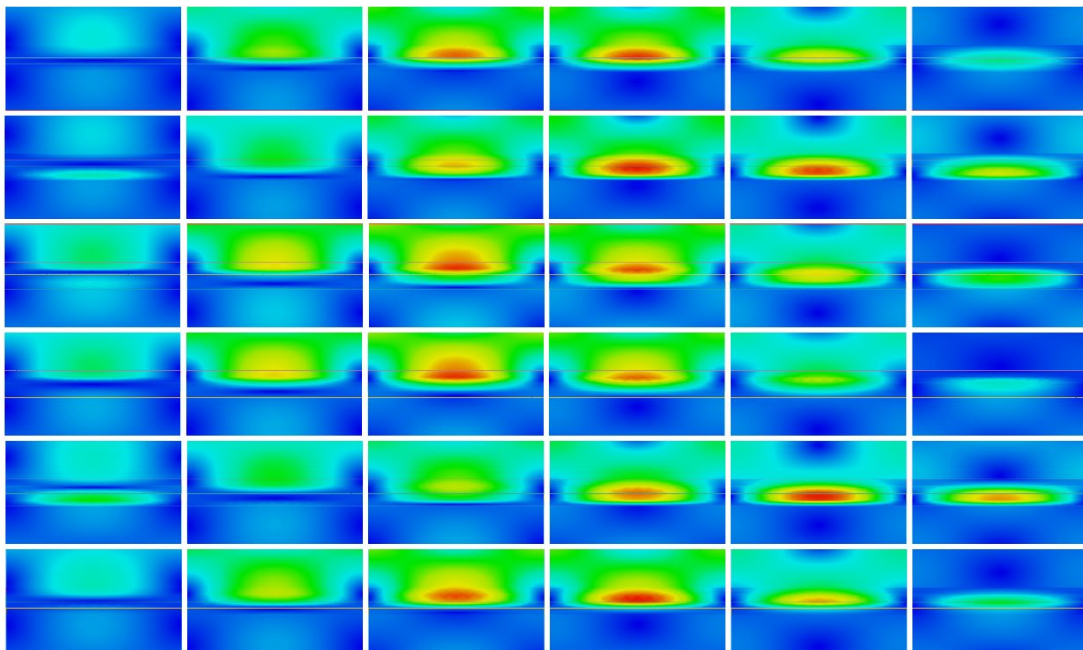


Fig. S17. The magnetic field diagrams for TCF1234, TCF1243, TCF1324, TCF1342, TCF1423, and TCF1432 are depicted from top to bottom. In the horizontal direction, the phase of the magnetic field ranges from  $0^\circ$  to  $150^\circ$  on the far left, with an increment of  $30^\circ$  between each graph.

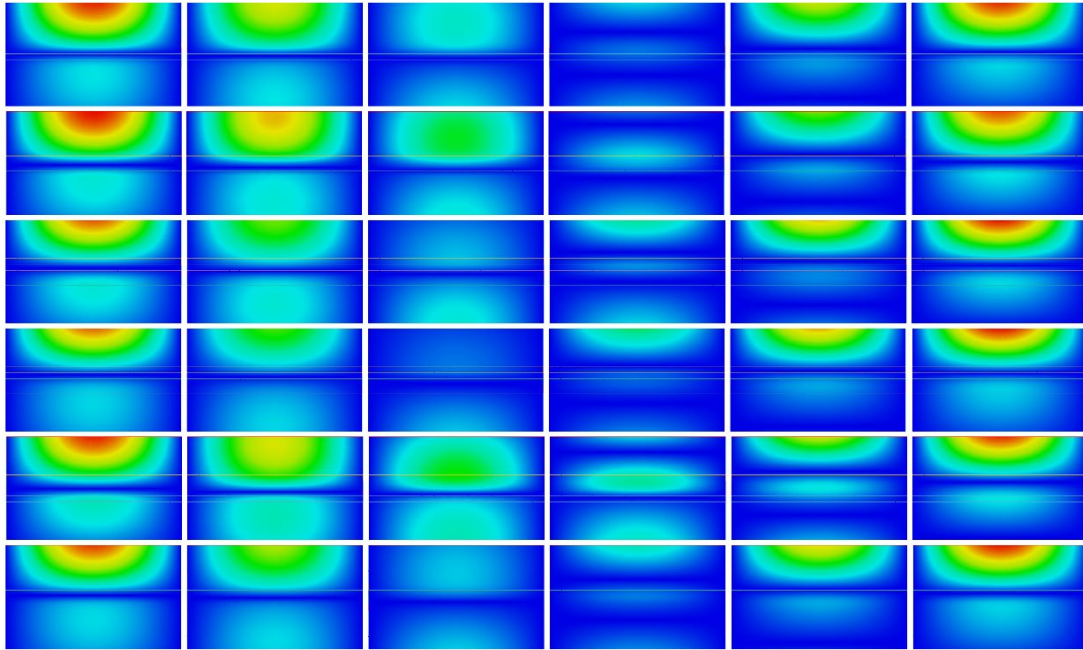


Fig. S18. The electric field diagrams for TCF2134, TCF2143, TCF2314, TCF2341, TCF2413, and TCF2431 are depicted from top to bottom. In the horizontal direction, the phase of the electric field ranges from  $0^\circ$  to  $150^\circ$  on the far left, with an increment of  $30^\circ$  between each graph.

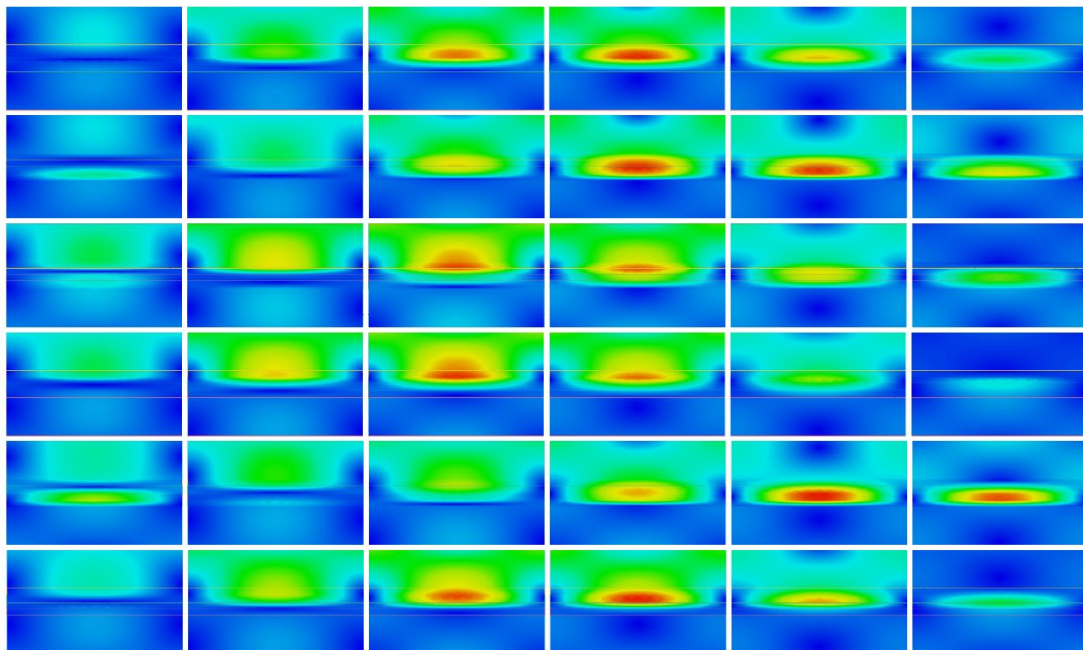


Fig. S19. The magnetic field diagrams for TCF2134, TCF2143, TCF2314, TCF2341, TCF2413, and TCF2431 are depicted from top to bottom. In the horizontal direction, the phase of the magnetic field ranges from  $0^\circ$  to  $150^\circ$  on the far left, with an increment of  $30^\circ$  between each graph.

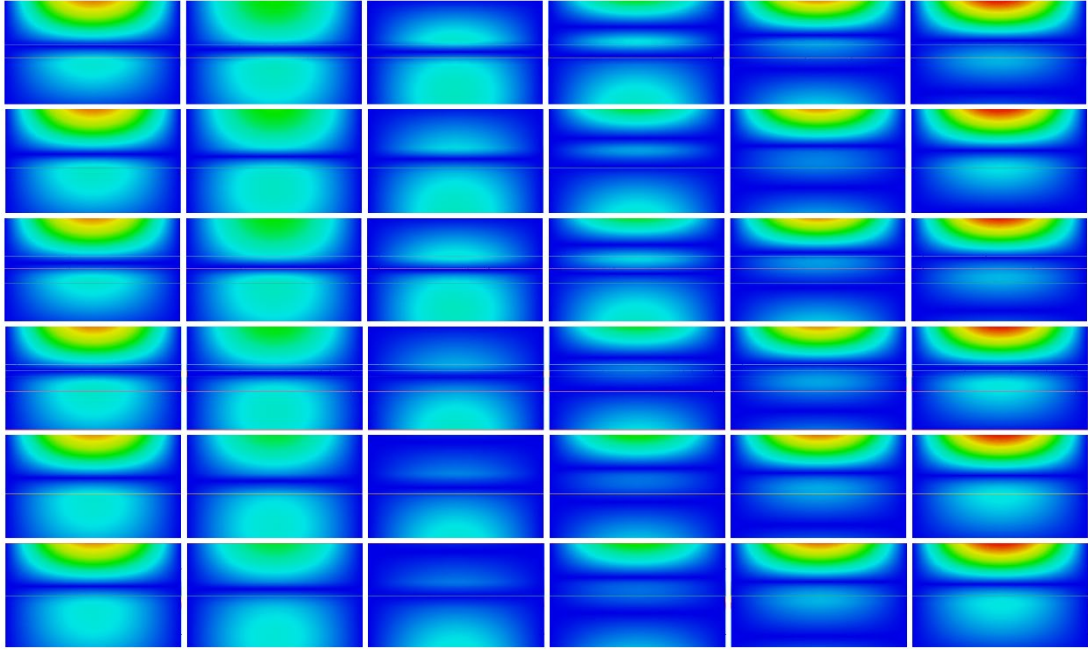


Fig. S20. The electric field diagrams for TCF3124, TCF3142, TCF3214, TCF3241, TCF3412, and TCF3421 are depicted from top to bottom. In the horizontal direction, the phase of the electric field ranges from  $0^\circ$  to  $150^\circ$  on the far left, with an increment of  $30^\circ$  between each graph.

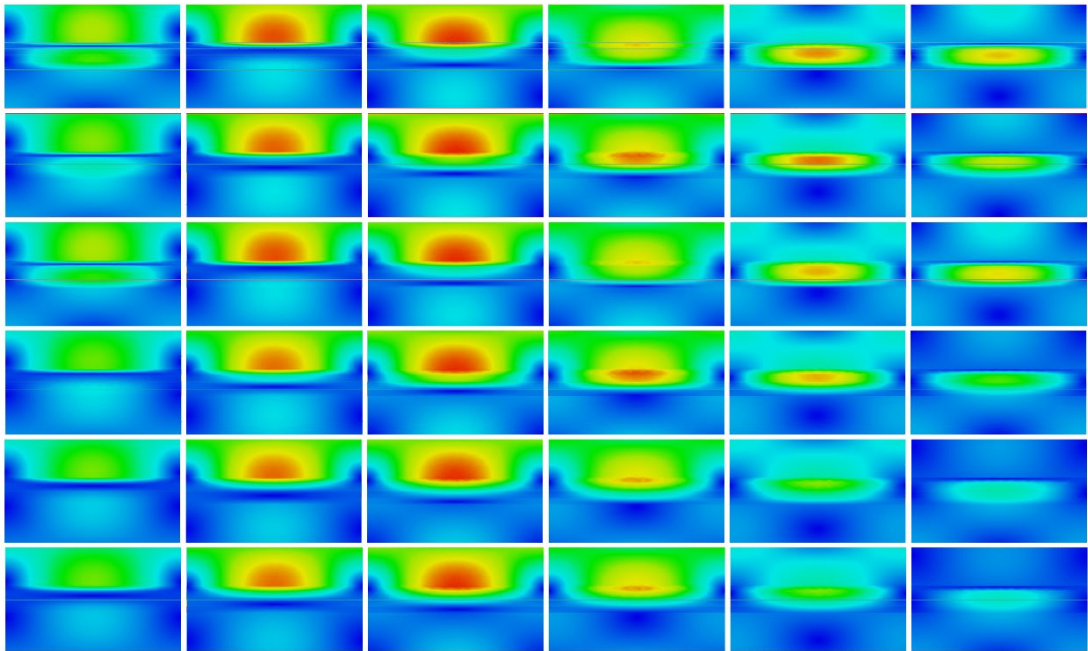


Fig. S21. The magnetic field diagrams for TCF3124, TCF3142, TCF3214, TCF3241, TCF3412, and TCF3421 are depicted from top to bottom. In the horizontal direction, the phase of the magnetic field ranges from  $0^\circ$  to  $150^\circ$  on the far left, with an increment of  $30^\circ$  between each graph.

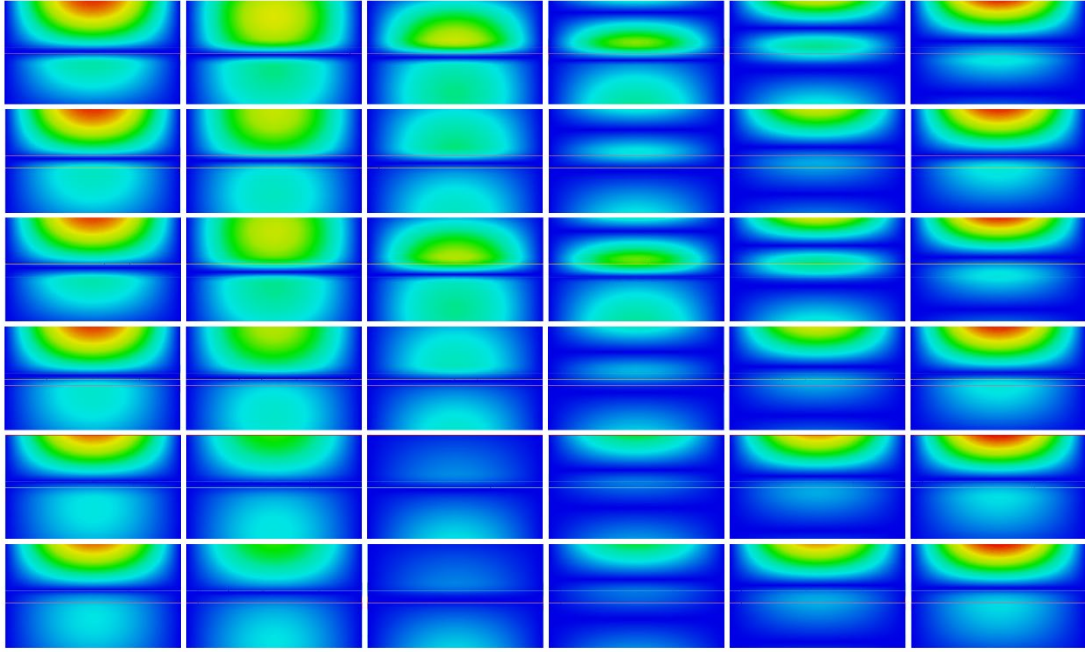


Fig. S22. The electric field diagrams for TCF4123, TCF4132, TCF4213, TCF4231, TCF4312, and TCF4321 are depicted from top to bottom. In the horizontal direction, the phase of the electric field ranges from  $0^\circ$  to  $150^\circ$  on the far left, with an increment of  $30^\circ$  between each graph.

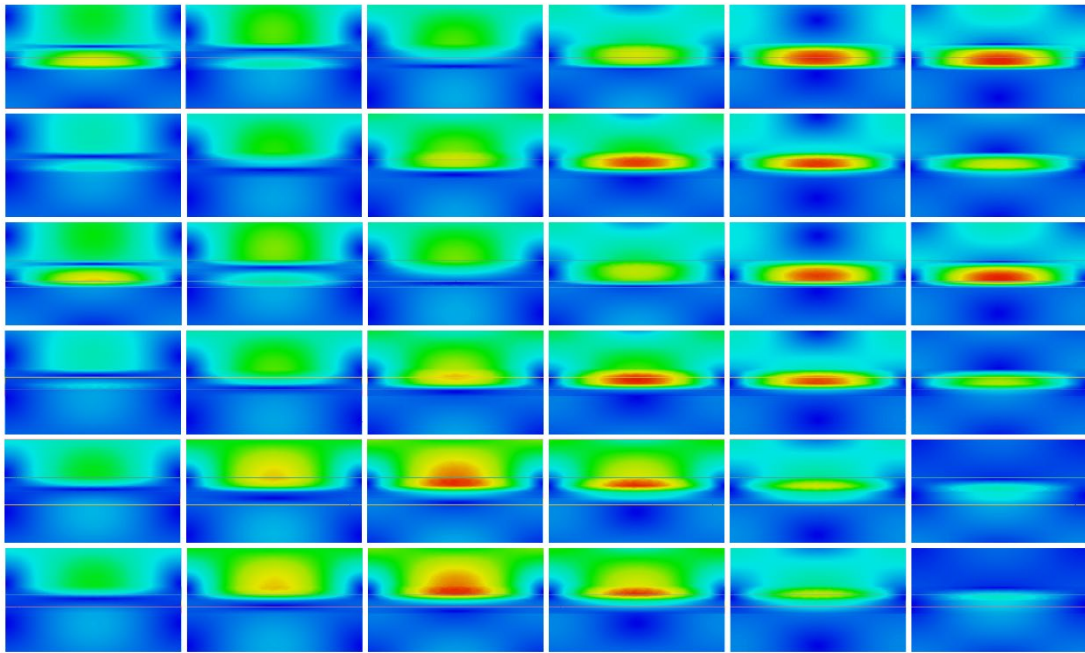


Fig. S23. The magnetic field diagrams for TCF4123, TCF4132, TCF4213, TCF4231, TCF4312, and TCF4321 are depicted from top to bottom. In the horizontal direction, the phase of the magnetic field ranges from  $0^\circ$  to  $150^\circ$  on the far left, with an increment of  $30^\circ$  between each graph.

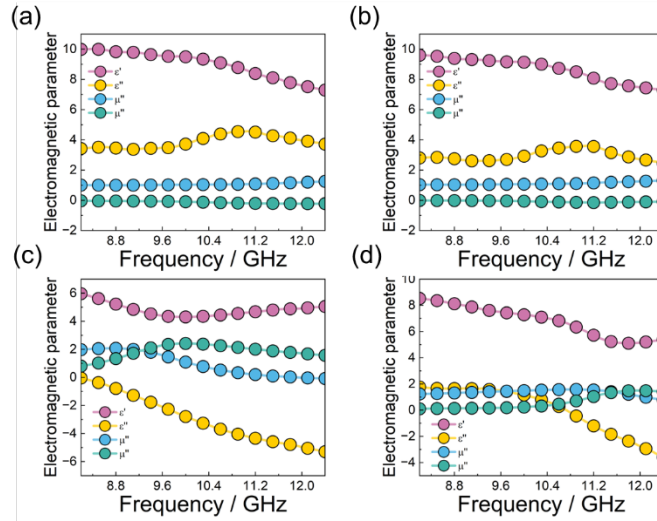


Fig. S24. EM parameters tested by waveguide method.

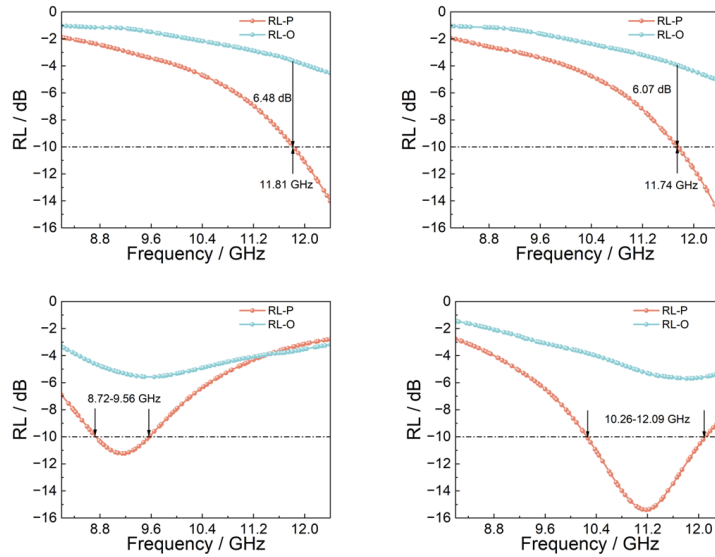


Fig. S25. Comparison of the RL values of the TCF films with superior performances. Positive reflection loss (RL-P) and Opposite reflection loss (RL-O) correspond to S11 and S22 respectively.

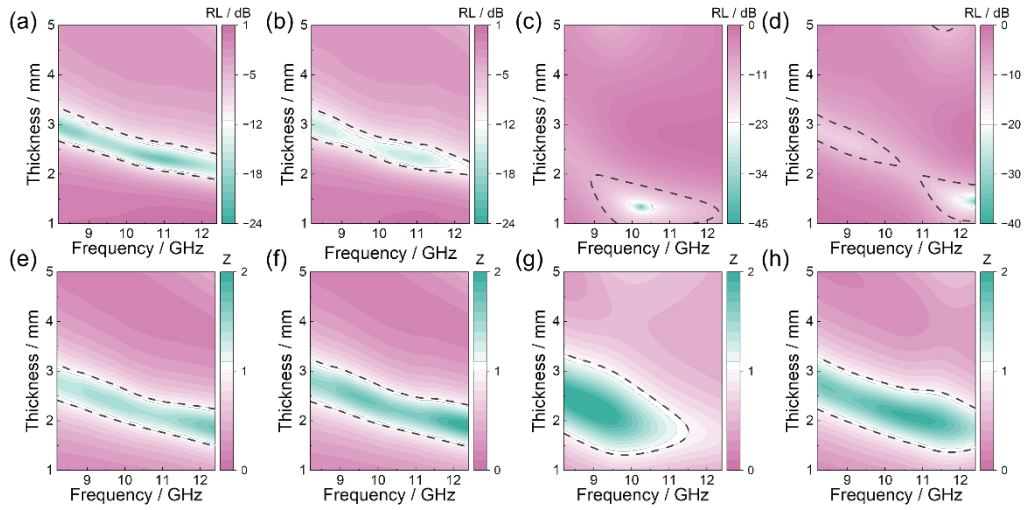


Fig. S26. (a-d) RL and (e-h) IM of TCF1423, TCF2413, TCF4123, TCF4213.

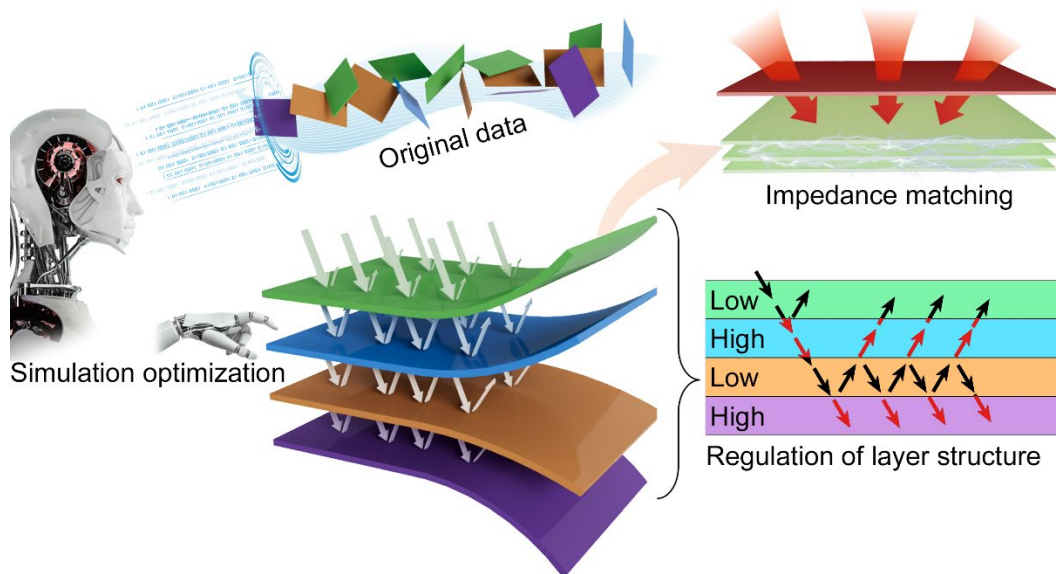


Fig. S27 Mechanism diagram of impedance gradient design.